E3S Web of Conferences **146**, 05002 (2020) https://doi.org/10.1051/e3sconf/202014605002
SCA 2019

Storing CO_2 as solid hydrate in shallow aquifers: Electrical resistivity measurements in hydrate-bearing sandstone

Jarand Gauteplass*, *Stian* Almenningen, and *Geir* Ersland

Department of Physics and Technology, University of Bergen, 5007 Bergen, Norway

Abstract. A recent proposed carbon dioxide (CO_2) storage scheme suggests solid CO_2 hydrate formation at the base of the hydrate stability zone to facilitate safe, long-term storage of anthropogenic CO_2. These high-density hydrate structures consist of individual CO_2 molecules confined in cages of hydrogen-bonded water molecules. Solid-state storage of CO_2 in shallow aquifers can improve the storage capacity greatly compared to supercritical CO_2 stored at greater depths. Moreover, impermeable hydrate layers directly above a liquid CO_2 plume will significantly retain unwanted migration of CO_2 toward the seabed. Thus, a structural trap accompanied by hydrate layers in a zone of favorable kinetics are likely to mitigate the overall risk of CO_2 leakage from the storage site. Geophysical monitoring of the CO_2 storage site includes electrical resistivity measurements that relies on empirical data to obtain saturation values. We have estimated the saturation exponent in Archie's equation, $n \approx 2.1$ (harmonic mean) for CO_2 and brine saturated pore network, and for hydrate-bearing seal ($S_H < 0.4$), during the process of storing liquid CO_2 in Bentheimer sandstone core samples. Our findings support efficient trapping of CO_2 by sedimentary hydrate formation and show a robust agreement between saturation values derived from PVT data and from modifying Archie's equation.

1 Introduction

Carbon capture and storage (CCS) technologies are expected to play a substantial role in the transformation of the energy sector toward reduced emissions of anthropogenic greenhouse gases [1]. Captured CO_2 is typically injected and stored in a supercritical state [2] in aquifers and depleted reservoirs at great depths. Once injected, CO_2 is retained in the sediments by physicochemical processes including structural trapping, capillary trapping, fluid dissolution, and mineral reactions. The contribution from each trapping process varies greatly with time [3]. Structural and capillary trapping are highly relevant from the onset of injection, while fluid dissolution and mineral reaction are believed to have a significant impact at a later stage.

More recently, an additional trapping mechanism suggests liquid CO_2 stored and contained by an upper CO_2 hydrate layer located at the base of the gas hydrate stability zone (GHSZ). This self-sealing hydrate layer makes an artificial cap rock that can prevent upward migration of CO_2 [4,5]. Cooler storage conditions enhances the CO_2 storage capacity due to increased CO_2 density, increased mobility control (important if long inter-well distance), and increased CO_2 solubility in water compared to storage of supercritical CO_2.

Experimental work has verified that CO_2 hydrate can form at the base of the GHSZ and reduce the CO_2 diffusion rate significantly in unconsolidated media [6]. Furthermore, high-density storage of CO_2 hydrate in silica sand has been demonstrated [7], as well as CO_2 hydrate acting as permeability barriers and successfully sealing off the pore space [8,9]. CO_2 immobilization by hydrate formation was directly visualized using MRI and micromodels [10]. A substantial GHSZ is ideal to make sure escaped liquid CO_2 is immobilized and converted to solid hydrate before reaching the seabed, and thus extending the hydrate sealing layer. Predicted thickness of the GHSZ for offshore Western Europe is nearly 0.5 km of the upper sediments [11], showing great potential for liquid CO_2 storage at shallow depths.

Resistivity measurements are routinely used to determine presence of sedimentary hydrates both in the field and in the laboratory. However, relevant empirical data are needed for saturation quantifications. These can be obtained and calibrated based on controlled laboratorial experiments. For a medium with uniform cross-section transmitting a uniform flow of electric current, resistivity is found from:

$$R_t = Z\frac{A}{L}\cos(\theta) \tag{1}$$

where R_t is the bulk resistivity, Z is the measured impedance, A is the cross-sectional area of the sample, L is the length of the sample, and θ is the phase angle. The Formation Factor (F) relates empirically to porosity through [12]:

$$F = \frac{R_0}{R_w} = a\phi^{-m} \tag{2}$$

* Corresponding author: Jarand.Gauteplass@uib.no

where R_0 is the resistivity of a fully brine-saturated sample, R_w is the resistivity of the brine, ϕ is the porosity of the sample, m is the cementation exponent and a is the tortuosity factor. R_w is calculated using a standard conversion [13]:

$$R_w = 0.0123 + \frac{3647.5}{[C]^{0.955}} \quad (3)$$

where C is the ion content of brine. The R_w value is corrected for temperature variations by [14]:

$$R_w(2) = R_w(1) * \frac{(T_1 + 21.5)}{(T_2 + 21.5)} \quad (4)$$

where T_1 is ambient temperature and T_2 is sample temperature. The Resistivity Index (RI) that applies to sediments partially saturated with a non-conductive material such as oil, gas, or hydrate, is defined as:

$$RI = \frac{R_t}{R_0} = S_w^{-n} \quad (5)$$

where R_t is the measured bulk resistivity, S_w is the brine saturation and n is the saturation exponent.

Hydrate growth is accompanied by an effective reduction of the pore space as well as a salinity increase of the remaining brine that is not converted to solid hydrate. Both of these processes results in a continuous change in R_0 as hydrate grows, and a dynamic R_0* needs to be implemented in eq. 5. This R_0* is calculated from eq. 2 by adjusting R_w and ϕ as hydrate grows. R_w is found from eq. 3-4 by keeping track of the salinity increase during hydrate growth from PVT data. PVT data is also used to monitor the hydrate saturation during hydrate growth, and ϕ_{eff} is then found from the following relation:

$$\phi_{eff} = \phi(1 - S_H) \quad (6)$$

where S_H is the hydrate saturation. The cementation exponent m is calculated by eq. 2 when the sample (with known porosity) is completely filled with brine. This m is then assumed constant as hydrate grows in the pore space [15]. The tortuosity factor a is set to 1 to ensure that $R_w = R_0$ in the limiting case where $\phi \rightarrow 1$.

Finally, the saturation exponent n is derived during hydrate growth by a modified version of eq. 5:

$$\log\left(\frac{R_t}{R_0 *}\right) = -n \log S_w \quad (7)$$

The n is found as the slope when plotting the left side of eq. 7 as a function of $-\log S_w$.

The majority of hydrate resistivity studies presented are related to CH_4 hydrate in the context of mapping and production of natural gas through various dissociation processes [15-18]. To the best of the authors' knowledge, this paper presents the first reported resistivity measurements on sedimentary CO_2 hydrate. We provide the saturation exponent n during CO_2 injection into brine-filled cores and subsequent CO_2 hydrate formation. Saturation values derived from resistivity measurements are compared with PVT derived saturations to investigate the applicability of using resistivity measurements to monitor the evolving CO_2 hydrate seal in subsurface carbon storage.

2 Materials and methods

Homogenous and quartz-dominated Bentheimer sandstone (95.5% quartz, 2.0% kaolinite, 1.7% K-feldspar, 0.8% other [19]) was used in this study. Average porosity and absolute permeability were measured to 0.22 and 1.1 D, respectively. Twin samples, all with diameter of 5 cm and length 15 cm, were cleaned, dried at 70 °C for 24 hours, and fully saturated with brine (3.5 or 5.0 weight% NaCl) under vacuum. The brine-saturated cores were positioned in a core holder containing a rubber sleeve, fixed upstream end-piece, and floating downstream end-piece (see Fig. 1). A nitrogen-supported back-pressure regulator was connected downstream and an effluent sample collector measured brine production. A refrigerated circulator supplied the system with cooling fluid. Precise high-pressure pumps regulated overburden and pore pressure. The laboratory setup allowed pressure differences and bulk resistivity (Hewlett-Packard LCR-meter; 1 kHz, two-electrode setup) across the core sample to be logged.

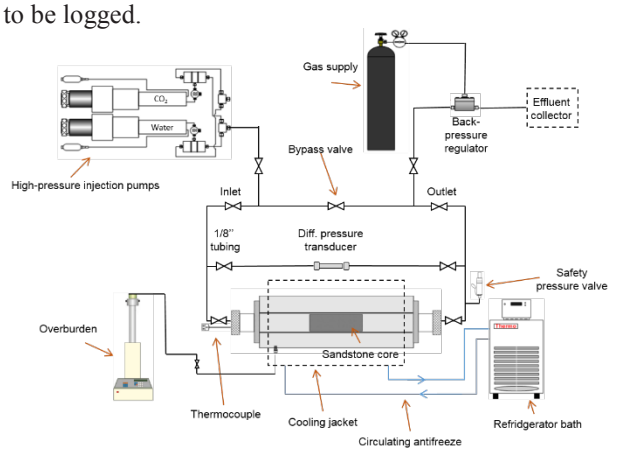

Fig. 1. Coreflooding laboratory setup including sandstone core sample, core holder, cooling system, pressure and temperature measurements, back-pressure regulator, and high-pressure pumps to regulate pore pressure and overburden. Modified from [20].

The pore space was pressurized with brine to 7.0 MPa, while the confinement pressure was set to 10.0 MPa. The core was then flooded with brine (μ=1.07 cP) over a range of injection rates and absolute permeability was calculated. The waterflood was followed by liquid CO_2 (μ=0.07 cP) injection at constant volumetric flow rate (0.5, 5 or 10 cm^3/min) to achieve a mixture of water and CO_2 in the pore space mirroring CO_2 invasion into an aquifer.

Two different hydrate growth conditions were designed in the laboratory: i) hydrate formation at constant pressure (CO_2 pressurized from both core ends,

bypass valve open) and ii) flow-induced hydrate formation during CO_2 injection with constant volumetric flow rate. Onset of hydrate formation within the pore space was determined from the increase in resistivity, temperature, and differential pressure.

3 Results and discussion

3.1 CO_2 – brine system (outside GHSZ)

The CO_2 injection rate into a porous media affects the displacement efficiency and fluid saturations within the pore network. Achieving substantial CO_2 storage capacity in a multiple well scenario relies on an efficient displacement process from injector to producer(s). Though supercritical CO_2 can recover about the same amount of water at core-scale, the more optimum mobility ratio between liquid CO_2 and water is likely to be important at long interwell distances.

Fig 2 shows the rate dependency on macroscopic sweep efficiency, which govern the initial fluid distribution before hydrate formation. Three experiments with CO_2 injection rate of 0.5 cm^3/min (circles), 5 cm^3/min (diamonds) and 10 cm^3/min (triangles) were conducted outside of the GHSZ (20 °C) at 7.0 MPa. Injection rate (capillary number) affects both overall S_w and pore-level fluid distribution. A linear production profile is valid before CO_2 breakthrough (BT), supplemented with water production measurements. Delayed CO_2 BT (indicated with broken vertical lines) for 5 and 10 cm^3/min implies improved sweep compared to the low injection rate (0.5 cm^3/min). However, doubling the injection rate from 5 to 10 cm^3/min had insignificant effect on the displacement process, reaching a plateau where approximately 50% of the brine remained after injecting several pore volumes (PV) of liquid CO_2. Though the experiments were designed to minimize capillary end effects by increasing the core length and using relatively high flow rates, the lowest rate (0.5 cm^3/min) experiment is prone to a more heterogeneous saturation profile due to reduced displacement efficiency. At breakthrough, saturation fractions in the pore space were S_w= 0.77 and S_{CO2}= 0.23 (0.5 cm^3/min), S_w= 0.59 and S_{CO2}= 0.41 (5 cm^3/min), and S_w= 0.57 and S_{CO2}= 0.43 (10 cm^3/min).

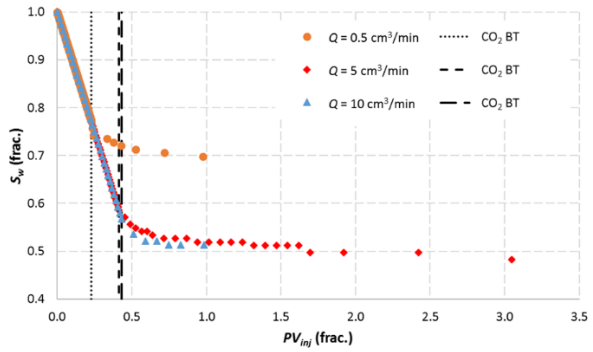

Fig 2. Drainage of initial water by liquid CO_2 in Bentheimer core samples at different injection rates; 0.5 cm^3/min, 5 cm^3/min, and 10 cm^3/min.

The bulk resistivity increased with increasing CO_2 saturation because electrically conductive brine was replaced by insulating CO_2 in the pore space. Fig 3 presents a logarithmic cross plot of water saturation (S_w) and resistivity index (RI) during CO_2 injection into the cores. The saturation exponent n was found as the slope of the curves, with emphasis on the first saturation point (S_w = 1) and the last saturation points (after CO_2 BT in the cores) when determining the slope of the curves (solid filled markers). The use of Archie's equation is not applicable until CO_2 has reached the end of the core, achieving a predominantly uniform two-phase saturation profile throughout the entire core length. This is illustrated by the data points (no fill) obtained before CO_2 BT, which deviate from the linear trend lines in Fig. 3.

The saturation exponent n increased with decreasing CO_2 flow rate, and was 1.9 for 10 cm^3/min, 2.1 for 5 cm^3/min, and 2.3 for 0.5 cm^3/min. This again reflects the different macroscopic sweep efficiencies that were achieved for the different flow rates, and highlights that n is sensitive to the displacement history. The n values identified in our CO_2-brine systems corroborate with n values reported for similar conditions [21,22]. CO_2 is a highly reactive fluid that can influence resistivity measurements through i) dissolution and dissociation where new ions are provided to the solution, and ii) contribution of surface conductivity – even in clay free rocks [21,23]. Both processes lead to increased electrolytic conductivity and may thus overestimate the water saturation if not accounted for. These effects are negligible if the water is highly saline [24]. In the next section, we will compare the water saturation derived from Archie's using the estimated n values with measured PVT data, to find if these effects are relevant to our systems with seawater salinity or higher.

3.2 CO_2 hydrate – brine system (within GHSZ)

To simulate the conditions of shallow CO_2 storage sites in offshore Western Europe, a temperature and pressure regime of 4 °C and 7.0 MPa pore pressure were chosen. This puts the system well within the GHSZ for CO_2 hydrate. Two hydrate growth scenarios were tested; i) static hydrate formation at constant pressure and ii) flow-induced hydrate formation under continuous CO_2 injection. Both approaches resulted in formation of CO_2 hydrate and subsequently immobilization of the injected CO_2 over a range of thermodynamic conditions.

Fig 4 shows a logarithmic cross plot of water saturation (S_w) and resistivity index (RI) during CO_2 hydrate formation in the pore space. The saturation exponent n is derived from the slope of the best-fit linear model to all measured data points during CO_2 hydrate formation. Final hydrate saturation depended on initial displacement of water by CO_2, and the more efficient displacement, the more hydrates were formed. Improved CO_2 sweep led to higher number of interfaces that acted as potential nucleation sites, and reduced water shielding in the samples. Increasing the initial CO_2 flow rate from 0.5 cm^3/min to 10 cm^3/min, increased the final hydrate saturation by almost a factor of 2.

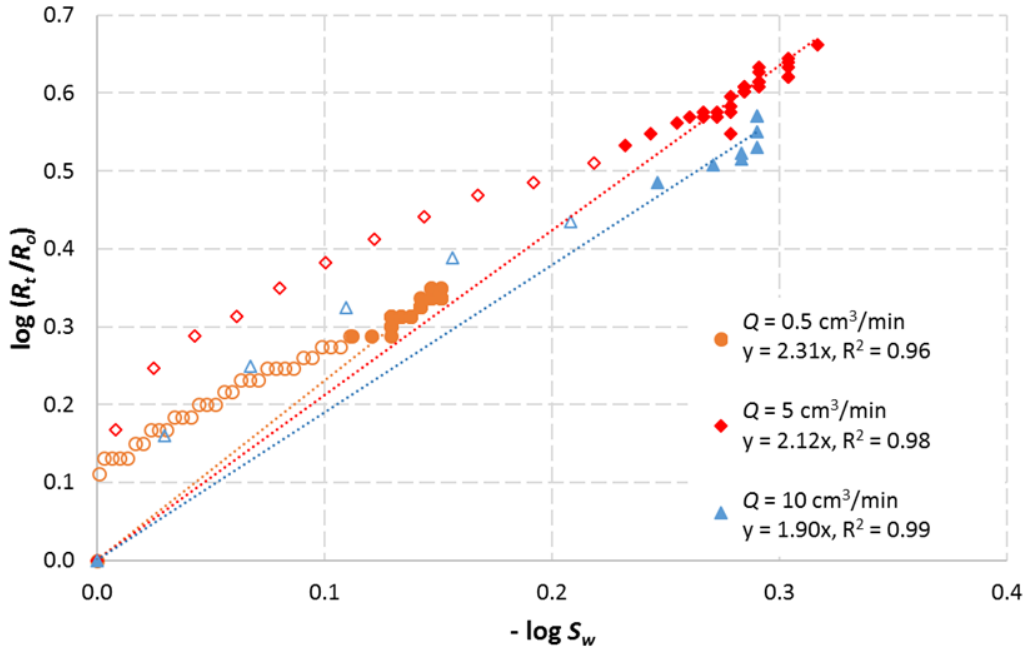

Fig 3. Logarithmic cross plot of RI and S_w during CO_2 injection in brine-filled Bentheimer core samples at injection rates: 0.5, 5 and 10 cm³/min at experimental conditions of 7.0 MPa and 20 °C. Data point markers with no fill (non-uniform saturation profile) were excluded from the linear trend lines. The saturation exponent n ranged between 1.9 – 2.3.

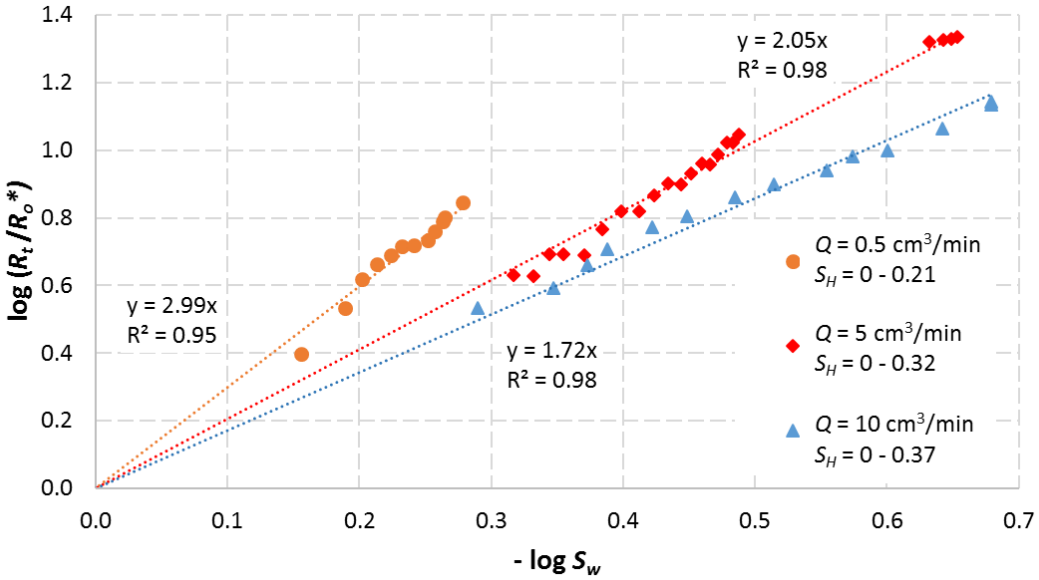

Fig 4. Logarithmic cross plot of RI and S_w during CO_2 hydrate formation in Bentheimer core samples from a range of initial brine saturations caused by varying CO_2 injection rates: 0.5, 5 and 10 cm³/min at 7.0 MPa and 4 °C. Depending on the saturation profiles, the saturation exponent n ranged from 1.7 to 3.0.

When hydrates, water and CO_2 were present simultaneously in the pore space, n corresponded to 1.7 for S_H = 0.37 (S_w = 0.21), 2.1 for S_H = 0.32 (S_w = 0.22), and 3.0 for S_H = 0.21 (S_w = 0.53). Compared to the CO_2-brine system, hydrate formation changed the n value for the 0.5 cm³/min drainage experiment (least uniform saturation distribution) from 2.3 to 3.0, for 10 cm³/min from 1.9 to 1.7, while for 5 cm³/min n remained unchanged (2.1). In the case of very limited hydrate formation (S_H = 0.21), low bulk resistivity measurements can be ascribed to substantial connectivity and increased ion content of the remaining free water. The obtained n values are nonetheless in good agreement with recent studies for natural gas hydrate in coarse-grained reservoirs [15], and for glass bead specimen [25].

The next three figures show a direct comparison of saturation values derived from Archie's and from measured PVT data.

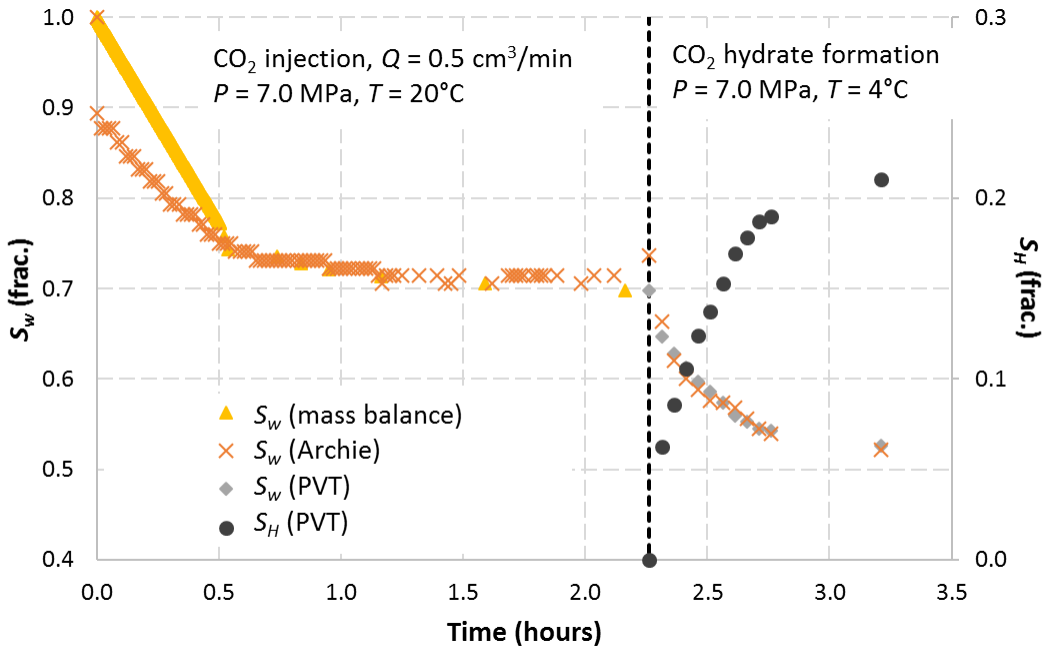

Fig 5. Comparison of saturation calculations from Archie and measured PVT data for injection rate 0.5 cm^3/min during initial displacement of water by CO_2 (7.0 MPa and 20 °C) and the following CO_2 hydrate formation (7.0 MPa and 4 °C). Obtained saturation values correlates very well after CO_2 breakthrough as a uniform saturation profile is established, and throughout CO_2 hydrate formation.

In Fig 5, saturation profiles during the initial displacement and the following hydrate nucleation and growth are displayed for flow rate 0.5 cm^3/min. The aforementioned unsteady-state regime occurring before CO_2 breakthrough, leads to severe deviation between the Archie saturation and correct linear displacement (mass balance) due to temporarily non-uniform saturation profiles. Once CO_2 breaks through at the outlet end of the sample, the saturation values from Archie's match actual PVT values very well at the plateau (S_w≈0.7). The onset of hydrate formation is indicated with a vertical line (broken). At this point, Archie's overestimate the water saturation somewhat compared to actual measurements. This apparent increase in water saturation is likely due to a short drop in resistivity linked to hydrate nucleation as reported in the literature [8,16,26]. Another possibility is the aforementioned CO_2 effects that may overestimate the water saturation, although the effects are most likely inhibited by the saline brine present. For the following hydrate growth process there is a very good agreement between the two water saturation profiles.

In Fig 6, drainage of water by CO_2 at injection rate of 5 cm^3/min and subsequent hydrate formation is displayed. Again, we observed a deviation in saturation profiles before CO_2 BT, and a good agreement after the CO_2 front reached the outlet end of the sample. The consistency continues from the onset of hydrate formation until hydrates occupy approximately 15% of the pore space. At this point the hydrate formation rate decreased substantially and the saturation profiles temporarily plateaued (for 0.2 hours). This period of hampered hydrate growth is not captured using Archie's saturation calculations, thus underestimating the water saturation here. Accelerated hydrate formation followed next and this "normalization" caused the end-point saturation values from PVT data and resistivity measurements to match once again.

Fig 7 shows saturation profiles during the initial displacement, and the following hydrate nucleation and growth for flow rate of 10 cm^3/min. The remaining water saturation in the core after CO_2 breakthrough was almost identical to the 5 cm^3/min experiment. There is a good agreement between the water saturation profiles after this point including the whole hydrate formation period in Fig 7.

CO_2 dissociation effects are highly sensitive to salinity. The 3.5 weight% NaCl solution used in Fig 5-7, belongs in a "high-salinity regime" where the conductivity was actually reduced by up to 15% due to reduced ion mobility [27]. This CO_2 dissolution effect, if not accounted for, will underestimate the water saturation derived from resistivity measurements. At the time-scale investigated in our study, no consistent impact of CO_2 dissociation on resistivity measurements was observed. Modifying Archie's equation by accounting for reduced effective porosity and increased salinity of the remaining water for each time step [16], resulted in resistivity saturation values agreeing very well with obtained PVT measurements.

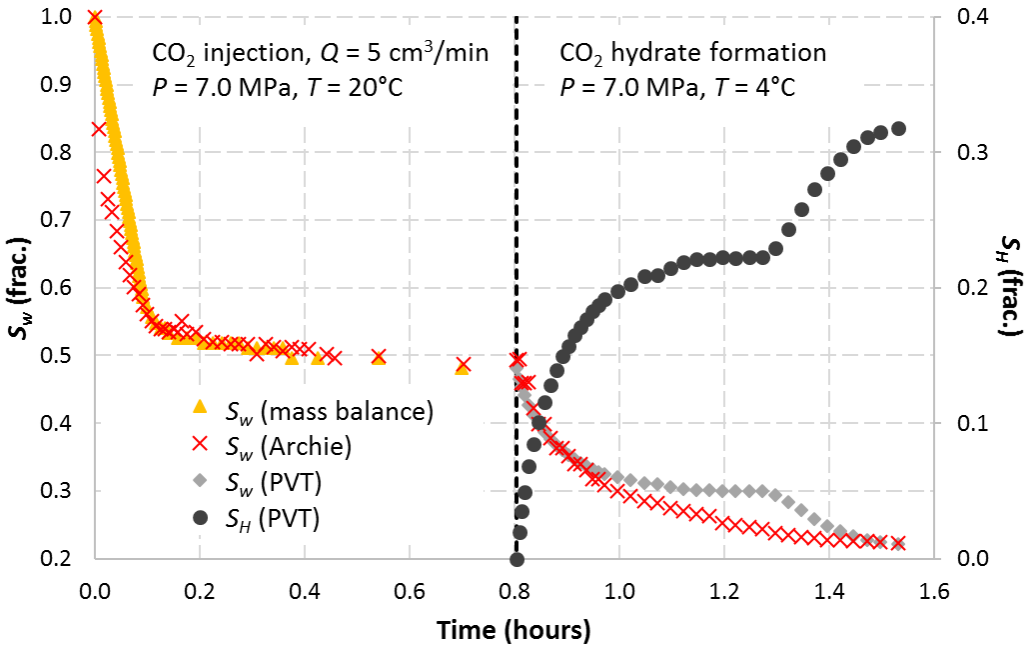

Fig 6. Comparison of saturation values obtained from Archie and measured PVT data for injection rate 5 cm^3/min during drainage (7.0 MPa and 20 °C) and during the following CO_2 hydrate formation (7.0 MPa and 4 °C).

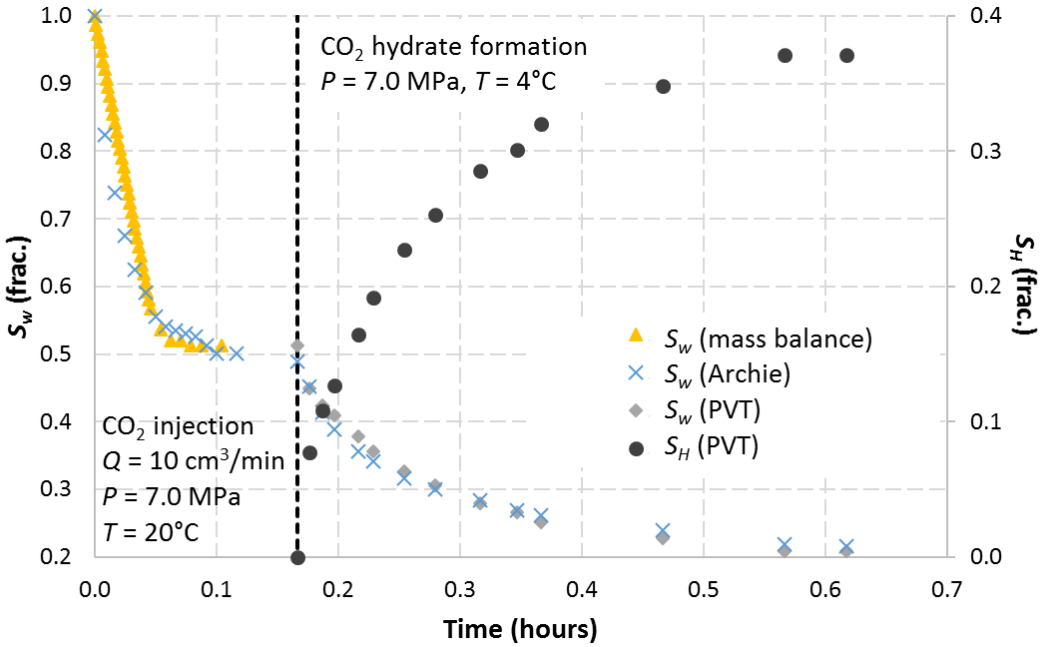

Fig 7. Comparison of saturation calculations from Archie and measured PVT data for injection rate 10 cm^3/min during initial displacement of water by CO_2 (7.0 MPa and 20 °C) and the subsequent CO_2 hydrate formation (7.0 MPa and 4 °C).

In addition to the constant pressure experiments, a series of flow-induced CO_2 hydrate formation experiments were tested for various thermodynamic conditions (within the GHSZ). CO_2 was injected into fully brine-saturated core samples at 7.0 MPa pore pressure and aquifer temperature of 4 °C or 6 °C. In Fig 8, resistivity profiles for different CO_2 flow rates, and salinity and temperature regimes are compared as a function of time. Here, increased flow rate (from 0.5 to 5 cm^3/min) accelerated hydrate formation and subsequent CO_2 trapping and immobilization. However, in terms of pore volumes (PV) CO_2 injected, we observed no effect of injection rate on hydrate induction time. The initial displacement of brine by liquid CO_2 increased the bulk resistivity from approximately 5 Ωm to 10 Ωm in all four corefloods. Two experiments were flooded with CO_2 at a constant rate of 5 cm^3/min at 7.0 MPa and 4 °C, where one core contained 3.5 weight% NaCl (red curve) and the other 5 weight% NaCl (yellow) – to demonstrate the effect of salinity increase on hydrate formation. Furthermore, two experiments were flooded with CO_2 at a constant rate of 0.5 cm^3/min at 7.0 MPa and salinity of 3.5 weight% NaCl, one experiment at 4 °C (blue) and the other at 6 °C (light blue) - to demonstrate the effect of temperature increase.

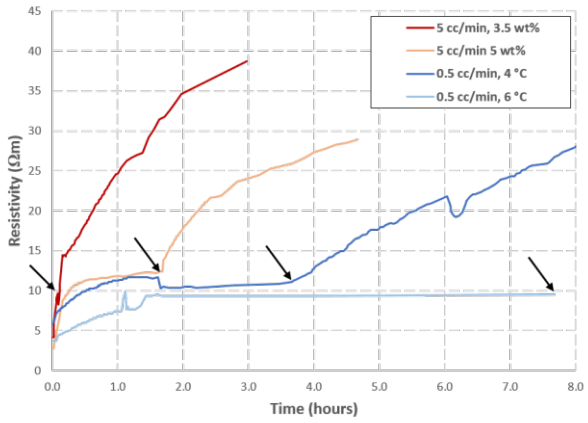

Fig 8. Resistivity profiles for various temperature and salinity conditions. Arrows indicate hydrate nucleation detected by a combination of pressure, resistivity, and temperature readings. Increase in salinity/temp caused a delayed CO_2 hydrate seal formation during continuous flow experiments.

The 5 cm^3/min constant rate experiment at lowest salinity (Fig 8 – red curve) started forming solid hydrates in the pore space shortly after CO_2 breakthrough (nucleation indicated with black arrows). By increasing the brine salinity from 3.5 to 5 weight% (yellow curve), we observed a prolonged induction time of approx. 1.5 hours (factor 9 increase) from flow-induced hydrate formation. When injecting CO_2 at 0.5 cm^3/min at 3.5 weight%, the effect of increasing the sandstone temperature from 4 °C to 6 °C was a factor 2 increase in induction time from 3.8 hours (blue) to 7.6 hours (light blue – resistivity data beyond this point is missing, however point of hydrate nucleation was identified from pressure and temperature logs).

The flow-induced hydrate induction time was evidently sensitive to salinity and temperature variations, and must be taken into consideration when screening for potential carbon storage sites. All four experiments led to solid CO_2 hydrate formation eventually. The steady increasing resistivity profiles after nucleation demonstrated hydrate growth in the pore network and decreased effective porosity and permeability. All corefloods experienced significant differential pressure build-up across the samples after hydrate formation, effectively stopping the CO_2 production at the outlet. These observations suggest that the injected CO_2 phase is made discontinuous by pore-spanning hydrate layers acting as permeability barriers, and thus successfully obstruct viscous CO_2 flow in the core sample for the time investigated.

Conclusions

Electrical resistivity measurements providing fluid saturations relevant for CO_2 hydrate storage, resulted in the following key experimental observations:

For two-phase CO_2-brine systems, the saturation exponent n ranged from 1.9 – 2.3 (harmonic mean $n \approx 2.1$) depending on the CO_2 injection rate used during the drainage process. Because the saturation exponent is sensitive to the saturation profile along the core length, it is not recommended to rely on saturation values derived from resistivity measurements using a 2-electrode setup in non-uniform fluid distribution processes.

During CO_2 hydrate formation, the saturation exponent n ranged from 1.7 – 3.0 (harmonic mean $n \approx 2.1$) depending on the initial distribution of brine, which resulted in different final CO_2 hydrate saturations. The estimated values of n may be used to map the brine saturation S_w and the CO_2 hydrate saturation ($S_H = 1 - S_w$) in excess water conditions, and are in good agreement with previously measured n values during methane hydrate growth. Resistivity measurements are increasingly important for $S_H < 0.4$, as acoustic methods currently cannot obtain sufficient velocity contrasts in zones of low hydrate saturation.

CO_2 hydrates effectively blocked the CO_2 flow path and sealed off the sandstone pore network during flow-induced hydrate formation for different injection rates and thermodynamic conditions. Moderate increase in brine salinity or aquifer temperature resulted in significantly prolonged induction time before CO_2 hydrate formed under constant flow rate. Once stored, unwanted CO_2 re-mobilization/migration was obstructed by formation of sedimentary hydrate layers. This observed mechanism could act as an additional safety factor against leakage from geological stored CO_2 located below the gas hydrate stability zone.

The authors gratefully acknowledge financial support from Equinor and the Research Council of Norway. One of the authors is supported by CLIMIT grant number 255490.

Nomenclature

a = tortuosity constant
A = area, L^2, m^2
C = ion content of brine, ppm
F = formation factor
L = length, L, m
m = cementation exponent
n = Archie's saturation exponent
RI = resistivity index
R_o = resistivity of fully water saturated sample, $(mL^3)/(tq^2)$, Ωm
R_t = resistivity of sample, $(mL^3)/(tq^2)$, Ωm
R_w = resistivity of brine, $(mL^3)/(tq^2)$, Ωm
S_{CO2} = saturation of CO_2, fraction
S_H = saturation of hydrate, fraction
S_w = saturation of water, fraction
S_{wi} = initial saturation of water, fraction
T = temperature, T, °C
Z = impedance, $(mL^2)/(tq^2)$, Ω
ΔP = differential pressure, $m/(Lt^2)$, bar
Θ = phase angle, °
φ = porosity, fraction
φ_{eff} = effective porosity, fraction
μ = viscosity, cP

References

1. International Energy Agency (IEA/OECD), "20 years of Carbon Capture and Storage - Accelerating future deployment." Review report (2016)
2. O. Eiken, P. Ringrose, C. Hermanrud, B. Nazarian, T. A. Torp and L. Høier, "Lessons learned from 14 years of CCS operations: Sleipner, In Salah and Snøhvit." Energy Procedia **4**, 5541-5548 (2011)
3. S. Benson and D. R. Cole, "CO2 Sequestration in Deep Sedimentary Formations." *Elements* **4**, 325-331 (2008)
4. H. Koide, M. Takahashi, H. Tsukamoto and Y. Shindo, "Self-trapping mechanisms of carbon dioxide in the aquifer disposal." *Energy Conversion and Management* **36**, 505-508 (1995)
5. K.Z. House, D.P. Schrag, C.F. Harvey and K.S. Lackner, "Permanent carbon dioxide storage in deep-sea sediments." *Proc Natl Acad Sci USA* **103**, 12291-12295 (2006)
6. B. Tohidi, J. Yang, M. Salehabadi, R. Anderson, and A. Chapoy, "CO2 hydrates could provide secondary safety factor in subsurface sequestration of CO2." *Environ. Sci. Technol.* **44**, 1509-1514 (2010)
7. M. Massah, D. Sun, H. Sharifi and P. Englezos, "Demonstration of gas-hydrate assisted carbon dioxide storage through horizontal injection in lab-scale reservoir." *Journal of Chemical Thermodynamics* **117**, 106-112 (2018)
8. J. Gauteplass, S. Almenningen, G. Ersland and T. Barth, "Hydrate seal formation during laboratory CO2 injection in a cold aquifer." *International Journal of Greenhouse Gas Control* **78**, 21-26 (2018)
9. J. Gauteplass, S. Almenningen, G. Ersland, T. Barth, J. Yang and A. Chapoy, "Multiscale investigation of CO2 hydrate self-sealing potential for carbon geo-sequestration." *Chemical Engineering Journal* **381**, 3122646 (2020)
10. S. Almenningen, J. Gauteplass, P. Fotland, G. L. Aastveit, T. Barth and G. Ersland, "Visualization of hydrate formation during CO2 storage in water-saturated sandstone." *International Journal of Greenhouse Gas Control* **79**, 272-278 (2018)
11. C. A. Rochelle, A. P. Camps, D. Long, A. Milodowski, K. Bateman, D. Gunn, P. Jackson, M. A. Lovell and J. Rees, "Can CO2 hydrate assist in the underground storage of carbon dioxide?" *Geological Society* **319**, 171-183 (2009)
12. G. E. Archie, "The Electrical Resistivity Log as an Aid in Determining Some Reservoir Characteristics." *AIME* **146**, 54-62 (1942)
13. Baker-Hughes. *Introduction to Wireline Log Analysis* (1992)
14. J. J. Arps, "The Effect of Temperature on the Density and Electrical Resistivity of Sodium Chloride Solutions." *Journal of Petroleum Technology* **5**, 17-20 (1953)
15. A. E. Cook and W. F. Waite, "Archie's Saturation Exponent for Natural Gas Hydrate in Coarse-Grained Reservoirs." *Journal of Geophysical Research: Solid Earth* **123**, 2069-2089 (2018)
16. K. A. Birkedal, G. Ersland, L. P. Hauge, A. Graue, K. Hester, J. Stevens and J. Howard, "Electrical resistivity measurements of CH4 hydrate-bearing sandstone during formation." *7th International Conference on Gas Hydrates* (2011)
17. A. E. Cook, B. I. Anderson, J. Rasmus, K. Sun, Q. Li, T. S. Collett and D. S. Goldberg, "Electrical anisotropy of gas hydrate-bearing sand reservoirs in the Gulf of Mexico." *Marine and Petroleum Geology* **34** (2012)
18. Y. F. Sun, and D. Goldberg, "Dielectric method of high-resolution gas hydrate estimation." *Geophysical Research Letters* **32** (2005)
19. T. Ramstad and H. Rueslåtten, "Pore scale numerical analysis for geological sequestration of CO_2." Technical report, 1-63 (2013)
20. C. Hågenvik, "CO2 Injection in Hydrate Bearing Sandstone with Excess Water." University of Bergen, MSc thesis (2013)
21. D. Bosch, J. Ledo, P. Queralt, F. Bellmunt, L. Luquot and P. Gouze, "Core-scale electrical resistivity tomography (ERT) monitoring of CO2–brine mixture in Fontainebleau sandstone." *Journal of Applied Geophysics* **130**, 23-36 (2016)
22. M. Han, S. Youssef, E. Rosenberg, M. Fleury and P. Levitz, "Deviation from Archie's law in partially saturated porous media: Wetting film versus disconnectedness of the conducting phase." *Physical Review E* **79** (2009)
23. J. H. Börner, V. Herdegen, J.-U. Repke and K. Spitzer, "The impact of CO2 on the electrical properties of water bearing porous media – laboratory experiments with respect to carbon capture and storage." *Geophysical Prospecting* **61**, 446-460 (2013)
24. M. Fleury and H. Deschamps, "Electrical Conductivity and Viscosity of Aqueous NaCl Solutions with Dissolved CO2." *Journal of Chemical & Engineering Data* **53**, 2505-2509 (2008)

25. E. Spangenberg and J. Kulenkampff., "Influence of methane hydrate content on electrical sediment properties." *Geophysical Research Letters* **33** (2006)
26. Y. Liu, W. Zhang, Y. Liu, S. Ren, "Experimental characterization and modelling of acoustic and electrical resistance in hydrate bearing sediments." *6th International Conference on Gas Hydrates* (2008)
27. J. H. Börner, K. Spitzer, J.-U. Repke and V. Herdegen, "The electrical conductivity of CO2-bearing pore waters at elevated pressure and temperature: a laboratory study and its implications in CO2 storage monitoring and leakage detection." *Geophysical Journal International* **203**, 1072-1084 (2015)